ACS OMEGA

http://pubs.acs.org/journal/acsodf

Article

Correlation Evaluation and Schematic Analysis of Influencing Factors Affecting Pore and Fracture Connectivity on the Microscale and Their Application Discussion in Coal Reservoir Based on X-ray CT Data

Huihuang Fang,* Zhangfei Wang, Shuxun Sang, Shiqi Liu, Chengchuan Gu, Jing Yang, Lei Li, and Yanhui Huang

Cite This: *ACS Omega* 2023, 8, 11852−11867

Read Online

ACCESS | Metrics & More | Article Recommendations

ABSTRACT: The connectivity of the pore/fracture system is the key to CO_2 injection and CH_4 production, which is of great significance in analyzing the correlation and weight of the influencing factors affecting the connectivity on the microscale. First, the 3D reconstruction of the coal reservoir is realized. Second, the characteristic parameters of pore/fracture structures are analyzed. Next, the characteristics of absolute permeability are analyzed, and then the correlation and weight analysis of the influencing factors are realized. Finally, the schematic analysis and application discussion of the influencing factors are carried out. The results show that porosity is the key factor restricting fluid migration. The heterogeneity of the reservoir can be characterized by the volume changes of the pore/fracture, organic matter, and mineral. The interconnected pores/fractures are mainly distributed in sheets and bands. The coordination number ranges from 1 to 15. The Ferret diameter is 0−10 μm. The tortuosity is 2.27111, 1.9034, 3.98522, and 3.51516, respectively, and the Euler characteristic number is 0.931868, 0.974719, 0.921144, and 0.897697, respectively. The permeability of the SH and YW samples is higher than that of the RL and PY samples. The single weight of the influencing factor is as follows: coordination number > Ferret diameter > Euler characteristic number > porosity > tortuosity. The analysis area of the comprehensive evaluation score of the influencing factors and the permeability value can be divided into three grades. There is a positive correlation among the coordination number, the quantity equilibrium of pores and throats, and the connectivity. The shape factor gradually increases with the increase of the Ferret diameter. The reservoir permeability is indirectly characterized by the coordination number, Ferret diameter, tortuosity, Euler characteristic number, and shape factor. This study can provide new ideas for clarifying the correlation degree and weight value of the characteristic parameters and can enrich the development of 3D digital core and CO_2-ECBM technology.

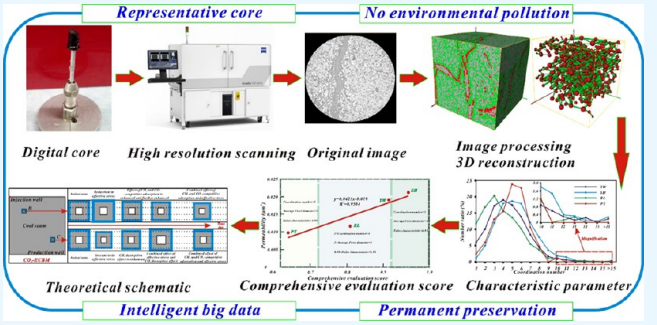

1. INTRODUCTION

As a complex porous medium, the pore/fracture system in the coal reservoir is the main enrichment site and the seepage channels of coalbed methane (i.e., CBM),[1] which not only restricts the gas-bearing capacity of CBM but also affects the recoverability of CBM.[2] Therefore, the connectivity of the pore/fracture system has always been the key factor affecting CO_2 injection and CH_4 production efficiencies, whether directly mining CBM or by CO_2 injection (i.e., CO_2-ECBM).[3] The pore/fracture system contains geometric and topological structures, and their core parameters include coordination number, Ferret diameter, Euler characteristic number, shape factor, and tortuosity.[4,5] It is a new research idea in the field of digital rock physics to discuss the influence of characteristic parameters of pore/fracture structures on self-connectivity from the perspective of pore/fracture structures.

The characterization methods of pore/fracture structures are summarized as follows: (1) pore size distribution: CO_2/N_2 adsorption method and mercury injection method;[6,7] (2) 2D morphology observation: optical microscopy and scanning electron microscopy;[8,9] (3) 3D imaging analysis: X-ray computed tomography (i.e., CT), focused ion beam scanning

Received: October 27, 2022
Accepted: March 10, 2023
Published: March 24, 2023

Figure 1. Sampling distribution of coal samples. The map of China was downloaded from Amap, and other photos were taken by Huanghui Fang. (a) YW, (b) SH, (c) RL, and (d) PY.

electron microscopy (i.e., FIB-SEM).[10,11] As a nondestructive and high resolution scanning technology, 3D imaging scanning is the most direct and accurate method to reconstruct the pore/fracture structure, which can realize the extraction and reconstruction of interconnected pores/fractures and the analysis of characteristic parameters of geometric and topological structures.[12,13] FIB-SEM can only analyze the nanoscale structures; the testing cost is high, and the testing period is long. Therefore, X-ray CT technology can be used to quantitatively analyze the pore/fracture structures and its characteristic parameters of the coal reservoir.

Considering the structural characteristics of the pore/fracture, there are many parameters affecting their connectivity. It is urgent to determine which parameters have positive or negative contributions to connectivity and to avoid overlapping evaluation results and nonunique calculation results in the process of single-parameter evaluation. Gray correlation analysis is a quantitative predictive analysis method,[11,14] that is, according to the gray system theory and method, the correlation degree between parent and child sequences and parameters is quantitatively analyzed, so as to avoid the problems mentioned above.[11,15] Based on this, and supplemented by the fuzzy comprehensive evaluation method, the weight value of each parameter affecting the connectivity of pore/fracture can be clarified. Therefore, the gray correlation analysis and fuzzy comprehensive evaluation methods can be adopted to evaluate the influence factors affecting the pore/fracture connectivity.

In this study, the Yuwu and Sihe collieries in the Qinshui basin and the Renlou and Panyi collieries in the Huainan and Huaibei coalfields were selected as the research areas. First, based on the basis of the data extracted by X-ray CT technology and the application of MATLAB software, the 3D reconstruction of the coal structure can be realized. Second, based on the basis of the extraction and reconstruction of the interconnected pores/fractures, the characteristic parameters of geometric and topological structures are analyzed. Then, the equivalent pore/fracture network model is used as the geological carrier to calculate the absolute permeability and analyze its characteristics. And then, based on gray correlation analysis and fuzzy comprehensive evaluation methods, the correlation and weight analysis of the influencing factors affecting pore/fracture connectivity are realized. Finally, the schematic analysis and application discussion of the influencing factors on the structural characteristics affecting pore/fracture connectivity are carried out.

The innovation of this research is mainly reflected in the following aspects: (1) Interconnected pore/fracture structures are reconstructed, and the equivalent network model is extracted. (2) Based on gray correlation analysis and fuzzy comprehensive evaluation methods, the correlation and weight analysis of the influencing factors affecting pore/fracture connectivity are realized. (3) The influence of structural parameters on pore/fracture connectivity and permeability evolution is discussed by schematic analysis and application discussion. This study can provide a theoretical basis for the study of permeability evolution during the direct production of CBM or CO_2 injection production and can enrich the development of 3D digital core and CO_2-ECBM technology.

2. SAMPLES AND METHODS

2.1. Sample Collection and Basic Testing. In this study, four samples collected are located in the Yuwu and Sihe collieries in Qinshui basin and the Renlou and Panyi collieries in Huainan and Huaibei coalfields, and the sample numbers are YW, SH, RL, and PY, respectively (Figure 1).[3,10,16] All samples were taken from the fresh working face, and the collection, packaging, and transportation were in accordance with national and international standards GB/T 6948−2008 and GB/T 8899−2013.[17,18] For the accuracy of subsequent experimental data, the samples collected should be treated with water and oxidation resistance as soon as possible (Figure 1).

Based on the vitrinite reflectance testing result (i.e., $R_{o,max}$ (%)) of experimental samples and the coal industry standard

https://doi.org/10.1021/acsomega.2c06943
ACS Omega 2023, 8, 11852−11867

Table 1. Key Properties of Coal Samples Used in This Study[a]

Sampling location	$R_{o,max}$ (%)	Proximate analysis (wt %)				Maceral concentrates (wt %)		
		M_{ad}	A_{ad}	V_{daf}	FC_{ad}	V_{it}	I_{ne}	M_{in}
YW	2.19	1.22	11.96	13.30	76.23	74.26	22.66	3.08
SH	3.33	1.48	13.12	6.32	81.39	79.84	18.36	1.80
RL	0.90	1.46	23.5	28.26	46.78	64.1	21.5	14.4
PY	0.89	1.46	13.5	18.36	66.68	55.53	27.25	17.22

[a]Notes: wt %, weight percent; $R_{o,max/\%}$, average maximum vitrinite reflectance; M_{ad}, moisture; A_{ad}, ash yield; V_{daf}, volatile matter; FC_{ad}, fixed carbon content; V_{it}, vitrinite content; I_{ne}, inertinite content; M_{in}, mineral content; ad, air-drying base; daf, dry ash-free basis.

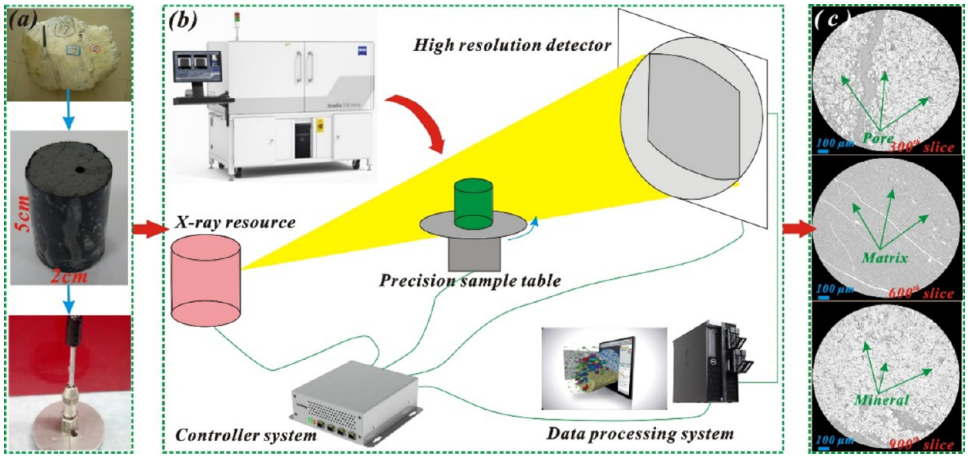

Figure 2. X-ray CT scanning system. (a) Preparation of sample, (b) imaging system components, (c) typical 2D CT slices of a coal sample.

MT/T1053−2008,[19] the YW and SH samples are anthracite and the RL and PY samples are bituminous coal. Other basic testing results of the four samples are shown in Table 1.

2.2. Sample Scanning and Visualization Reconstruction. In this study, the Xradia 520 Versa CT scanning system produced by Carl Zeiss was adopted for X-ray CT scanning. The system mainly consists of an X-ray source, a precision sample table, a high-resolution detector, a data processing and controller system, and other core components (Figure 2).[3,20] The density difference of components in the coal sample is the basis of the scanning test and visualization reconstruction.

The coal samples collected were prepared into cylinders of certain specifications according to the requirements of the scanning experiment for the testing company to complete further sample preparation and scanning work (Figure 1; Figure 2a). After X-ray CT scanning, 1000 slices with a size of nearly 990 × 1010 voxels were obtained for each of the four tested samples with a resolution of 1.00 μm (Table 2). After scanning, the black, gray, and white in typical slices represent pore/fracture, matrix, and mineral phases, respectively (Figure 2c).

Based on the typical slices obtained by scanning, the 3D reconstruction of coal reservoir can be completed. The core steps include the denoising of typical slices, the threshold selection and image segmentation, the analysis of representative volume element (RVE), the identification analysis of pore/fracture, and the construction of equivalent pore/fracture network model (Figure 3). The denoising process of the Median filter can protect the integrity of pores and smooth the transition between pores and matrixes, so as to distinguish pore/fracture from other components (Figure 3b).[21,22] The Watershed algorithm can be used for threshold selection of pore/fracture, matrix and mineral phases (Figure 3c).[3,23] The size of RVE can be determined by analyzing the variation law of porosity and RVE size (Figure 3-d).[24,25] The Maximum sphere algorithm can well capture the topological and geometric structures and its connectivity of pore/fracture spaces, and is often used to construct equivalent pore/fracture network model, and can further extract pores and throats (Figure 3f).[10,22] The principles, algorithms, and schematics of each core operation step can be found in the results published by our research team.[3,10,20]

Table 2. Dimensions of Four Coal Samples Used in This Study

Sample ID	Sample shape	Number of voxels	Voxel size (μm)
SH	Cylindrical type	987 × 1013 × 989	1.00
YW	Cylindrical type	988 × 1014 × 990	1.00
PY	Cylindrical type	988 × 1013 × 990	1.00
RL	Cylindrical type	987 × 1012 × 990	1.00

2.3. Schematic Diagram of Sample Connectivity Analysis. The spatial connectivity of the pore/fracture structure is important topological information on porous media, which affects their physical properties. If the pore phase is continuous from one end to the other in one direction, then it means that the digital coal is connected in this direction. The digital coal consists of a large number of discrete pixels, and the connectivity between pixels can be described in three ways: 6-connected, 18-connected, and 26-connected (Figure 4).[26,27] In this study, the connectivity analysis was mainly carried out by means of 6-connected processing; that is, the voxels with common faces were considered to be interconnected.

2.4. Schematic Diagram and Calculation of Characteristic Parameters of Pore and Fracture Structures. The structural characteristics of pore and fracture include geometrical and topological structures. The geometric character-

https://doi.org/10.1021/acsomega.2c06943
ACS Omega 2023, 8, 11852−11867

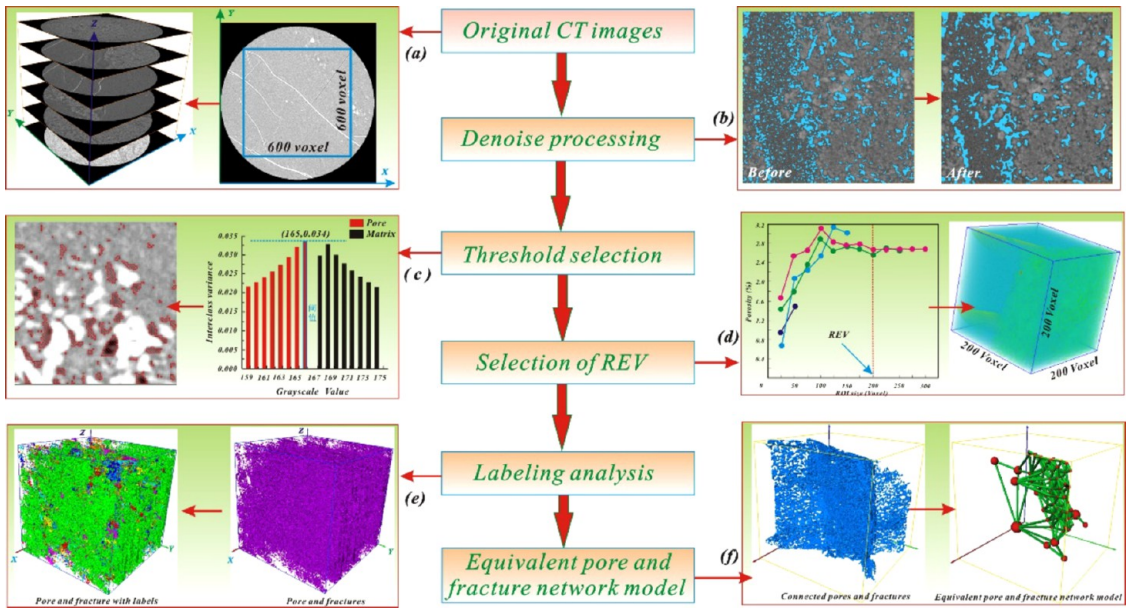

Figure 3. Schematic diagram of extraction process of pore and fracture model with labels. (a) Original CT images; (b) denoising processing; (c) threshold selection; (d) selection of REV; (e) labeling analysis; (f) equivalent pore and fracture network model.

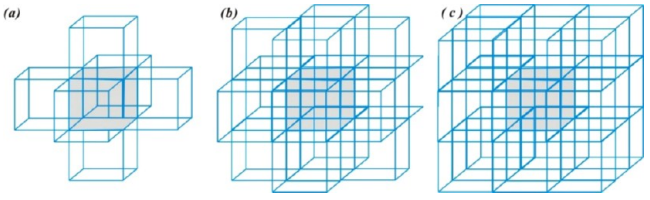

Figure 4. Schematic diagram of connectivity between pixels: (a) 6-connectivity; (b) 18-connectivity; (c) 26-connectivity.

istics mainly refer to the geometric size and shape distribution of pore and throat, and the core parameters include pore and throat radius, throat length, pore volume, shape factor, and tortuosity. The topological characteristics mainly refer to the correlation between the pore and throat, and the core parameters include coordination number and Euler characteristic number. In view of the correlation degree analysis of the interconnected pores/fractures and their influencing factors, the shape factor, tortuosity, coordination number, Euler characteristic number, Ferret diameter, and other parameters should be mainly discussed.

2.4.1. Shape Factor. Shape factor refers to the parameters that can quantitatively characterize pore and throat shape within the pore/fracture network model. As the cross-section shape of the pore and throat is not fixed in different directions, the cross-section area and circumference are constantly changing (Figure 5). Therefore, the shape factor of the pore and throat is the average of a series of sectional shape factors, which can be calculated by formula 1:

$$G = A_{p-t}/P_{p-t}^{2} \quad (1)$$

Where, A_{p-t} is the cross-sectional area of the pore and throat, m^2, and P_{p-t} is the cross-sectional circumference of the pore and throat, m.

2.4.2. Tortuosity. Tortuosity mainly describes the curvature of the pore and throat, which refers to the ratio between the actual length of the connected pores and the throats, and the shortest distance (Figure 6).[5,26] Tortuosity plays an important

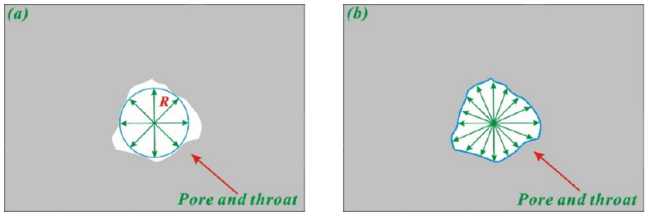

Figure 5. Schematic diagram of the calculation of the shape factor of pores and throats. (a) Processed pore radius; (b) processed pore cross-section.

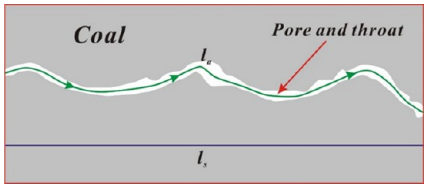

Figure 6. Schematic diagram of tortuosity.

role in controlling permeability and capillary resistance, which can be calculated by formula 2:

$$\tau = l_a/l_s \quad (2)$$

where l_a is the actual length of the connected pores and throats and l_s is the shortest distance between the connected pores and throats.

2.4.3. Coordination Number. Coordination number refers to the number of throats connected to each pore.[28,29] The coordination number plays an important role in controlling fluid flow and production in pores, and the larger the coordination number, the better the connectivity is. When the coordination number is 0, the pores have no connectivity and are called dead-ending pores.

2.4.4. Euler Characteristic Number. The Euler characteristic number is the connectivity function.[30] The closer the intersection point between the connectivity function and the X axis is to 0, the worse the connectivity of the pores in the

https://doi.org/10.1021/acsomega.2c06943
ACS Omega 2023, 8, 11852−11867

reservoir is. The Euler characteristic number can be calculated by formula 3:

$$\chi_v(r) = \frac{N_N(r) - N_C(r)}{V} \quad (3)$$

Where $N_N(r)$ represents the number of isolated pores with a pore radius greater than r, $N_C(r)$ represents the number of connected pores with a pore radius greater than r, and V is the volume of the pore network model analyzed.

2.4.5. Ferret Diameter. The Ferret diameter is not an actual diameter but a set of diameters determined by a set of two parallel tangent distances to the pore and fracture (Figure 7).[11]

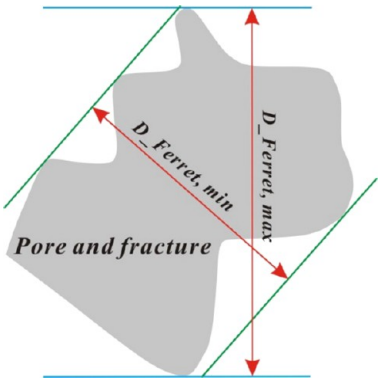

Figure 7. Schematic diagram of the Feret diameter.

The maximum (i.e., *D_Ferret,max.*) and minimum (i.e., *D_Ferret,min.*) Ferret diameters are more important for pore/fracture connectivity. The mean of ferret diameter (i.e., *D_Ferret,ave.*) is the mean of all ferret diameters in different directions (Figure 7).

2.5. Calculation Model and Boundary Condition Loading of Absolute Permeability. Absolute permeability can be defined as the measure of the ability of a porous material to transmit a single phase fluid.[31,32] The Stokes equations can be solved for numerically estimating the absolute permeability,[33,34] as can be seen in formula 4:

$$\begin{cases} \vec{\nabla}\cdot\vec{V} = 0 \\ \mu\nabla^2\vec{V} - \vec{\nabla}P = 0 \end{cases} \quad (4)$$

Where $\underset{\nabla\cdot}{\rightarrow}$ is the divergence operator; $\underset{\nabla}{\rightarrow}$ is the gradient operator; $\underset{V}{\rightarrow}$ is the velocity of the fluid in the fluid phase of the material; μ is still the dynamic viscosity of the flowing fluid; ∇^2 is the Laplacian operator; and P is the pressure of the fluid in the fluid phase of the material.

Once formula 4 is solved, Darcy's law can be applied to calculate the absolute permeability:[35,36]

$$\frac{Q}{S} = -\frac{k}{\mu}\frac{\Delta P}{L} \quad (5)$$

Where, Q is the global flow rate that goes through the porous medium, m^3/s; S is the cross section of the sample through which the fluid goes, m^2; k is the absolute permeability, m^2; μ is the dynamic viscosity of the flowing fluid, Pa s; P is the pressure applied around the sample, Pa; and L is the length of the sample core in the flow direction, m.

In this study, the specific boundary condition loading for calculating the absolute permeability is shown in Figure 8. The boundary conditions of the geometric model are set as follows: (1) the fluid material property is set as normal temperature methane. The density of methane in standard state is 0.717 kg/m^3 and the dynamic viscosity is 1.85×10^{-5} Pa s. (2) The inlet and outlet of fluid flow are set as two opposite surfaces, the pressure constraint is set as the boundary conditions of the inlet and outlet, and the boundary conditions of the other four surfaces are set as the no-slip surface. (3) The inlet pressure is set to 1.1 MPa, and the outlet pressure is set to 0.1 MPa (Figure 8).

2.6. Gray Correlation Analysis and Fuzzy Comprehensive Evaluation Analysis. In the process of analyzing the correlation degree and weight of each influence factor affecting the connectivity of pore/fracture, the analysis ideas are as follows: first, the evaluation parameters are selected and quantified. Second, the parent and child sequences are determined. Then, the gray correlation coefficient and gray

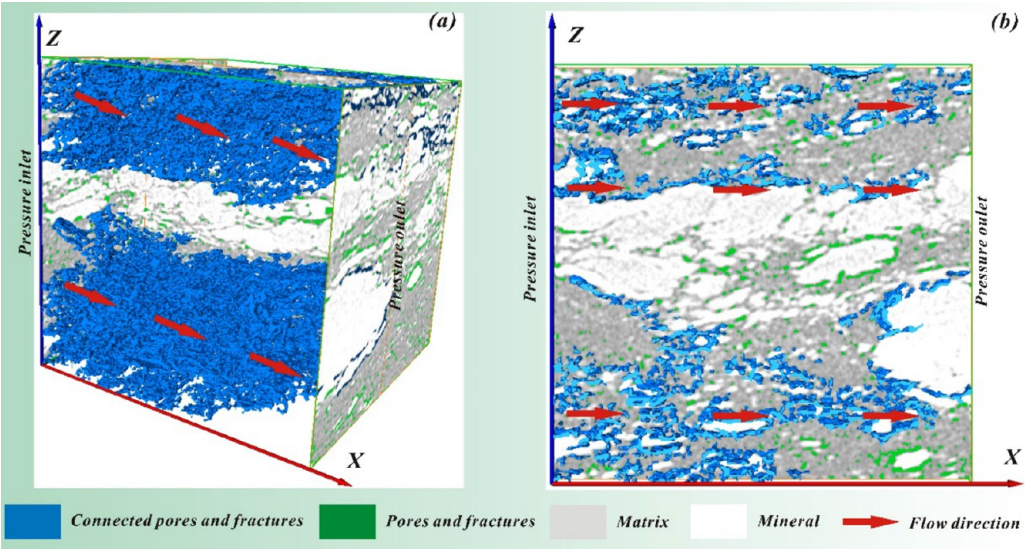

Figure 8. Schematic diagram of boundary condition setting. (a) Three-dimensional view; (b) two-dimensional plane view.

https://doi.org/10.1021/acsomega.2c06943
ACS Omega 2023, 8, 11852−11867

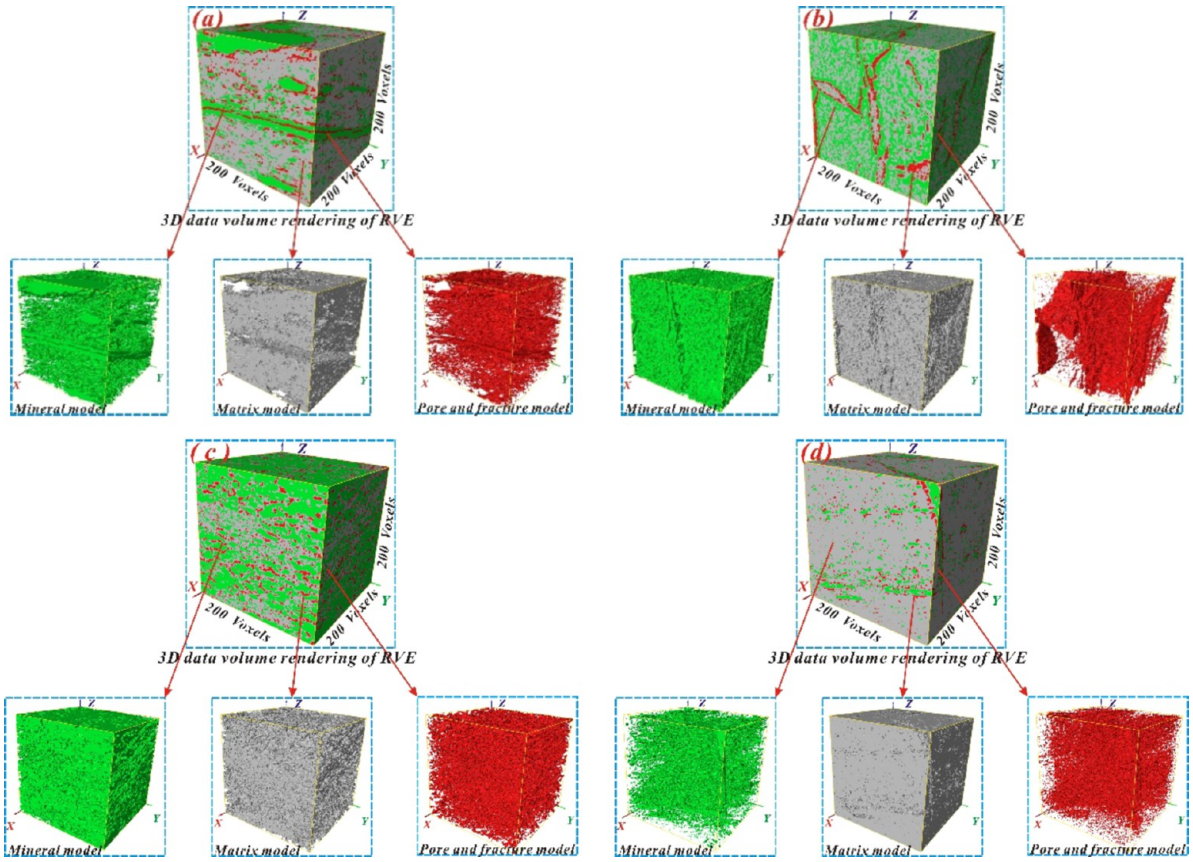

Figure 9. 3D visualization reconstruction of the coal sample. (a) YW sample; (b) SH sample; (c) RL sample; (d) PY sample.

correlation degree are calculated. Finally, the weight coefficient is determined by normalization processing.

2.6.1. Selection of Influencing Factors and Determination of Child and Parent Sequences. The reservoir permeability is closely related to the pore/fracture connectivity. From the perspective of structure characteristics, the connectivity can be represented by porosity, coordination number, tortuosity, Euler characteristic number, Ferret diameter, and other parameters.

Taking the above factors into consideration, the main factor is determined to be the parameter affecting the pore/fracture connectivity, that is, reservoir permeability. The main factor constitutes the parent sequence of correlation analysis, namely:

$$\{X_t^{(0)}(0)\},\ t = 1, 2, 3, \cdots, n \tag{6}$$

where t is the number of coal samples analyzed.

Child sequence refers to the sequence composed of all parameters affecting the connectivity of pore/fracture except the main factor, namely, porosity, coordination number, tortuosity, Euler characteristic number, and Ferret diameter:

$$\{X_t^{(0)}(i)\},\ i = 1, 2, 3, \cdots, m;\ t = 1, 2, 3, \cdots, n \tag{7}$$

where i is the number of parameters analyzed.

Considering all parameters and parent and child sequences of connectivity evaluation, the original data matrix for correlation analysis of influencing factors affecting connectivity can be formed, which can be shown below:

$$X^{(0)} = \begin{bmatrix} X_1^{(0)}(0) & X_1^{(0)}(1) & \cdots & X_1^{(0)}(m) \\ X_2^{(0)}(0) & X_2^{(0)}(1) & \cdots & X_2^{(0)}(m) \\ \vdots & \vdots & \vdots & \vdots \\ X_n^{(0)}(0) & X_2^{(0)}(1) & \cdots & X_n^{(0)}(m) \end{bmatrix} \tag{8}$$

2.6.2. Quantitative Processing of Parameters. In order to avoid the difference of physical meaning and dimension of the original data, the maximum standardization and normalization methods can be used to quantitatively analyze the original parameters. According to the difference in contribution degree of each influencing factor affecting connectivity, the quantification method is different. The processing methods of maximum standardization are different according to the different meanings of the parameters. For the parameters with a positive contribution to connectivity, the maximum value of the parameter is divided by the data of a single parameter. For parameters that have a negative contribution to connectivity, the maximum value of this parameter is first subtracted from the single parameter data, and then, the difference is divided by the maximum value of this parameter.

2.6.3. Gray Correlation Calculation. Gray correlation coefficient (i.e., $\xi_{i,0}$) can be used to comprehensively analyze the relationship between primary and secondary factors, so as to get the correlation degree between parent and child sequences.

$$\xi_{i,0} = \frac{\Delta\min + \rho\Delta\max}{\Delta_t(i, 0) + \rho\Delta\max},\ i = 1, 2, 3, \cdots, m \tag{9}$$

https://doi.org/10.1021/acsomega.2c06943
ACS Omega 2023, 8, 11852−11867

Table 3. Results of Coal Sample Component Content Calculation

	Pore and fracture model		Matrix model		Mineral model	
Sample ID	Voxel count	Volume fraction (%)	Voxel count	Volume fraction (%)	Voxel count	Volume fraction (%)
YW	853 596	10.67	4 849 361	60.62	2 297 043	28.71
SH	714 935	8.94	4 037 877	50.47	3 247 186	40.59
RL	850 167	10.63	2 855 774	35.70	4 294 059	53.68
PY	470 390	5.88	6 779 113	84.74	750 497	9.38

Where

$$\Delta_t(i, 0) = |X_t^{(1)}(i) - X_t^{(1)}(0)| \quad (10)$$

$$\Delta\max = \max_t \max_t |X_t^{(1)}(i) - X_t^{(1)}(0)| \quad (11)$$

$$\Delta\min = \min_t \min_t |X_t^{(1)}(i) - X_t^{(1)}(0)| \quad (12)$$

Considering the accuracy of data analysis and the distinctness of evaluation effect, the resolution coefficient, ρ, generally $\rho \in [0,1]$, can be introduced into the gray correlation coefficient processing. In this analysis, $\rho = 0.5$ was taken.

The calculation formula of gray correlation degree (i.e., $r_{i,0}$) is as follows:

$$r_{i,0} = \frac{1}{n}\sum_{t=1}^{n} \xi_{i,0} \quad (13)$$

The degree value of gray correlation is between 0 and 1. The closer the calculated value is to 1, the higher the correlation degree of parent and child sequences is. The correlation degree can not only reflect the influence of each characteristic parameter itself on the connectivity but also reflect the internal laws implied between each parameter.

2.6.4. Determination of Weight Coefficient. To determine the weight coefficient (i.e., a_i), it is necessary to consider the weight of the child sequence to the parent sequence and then analyze the contribution of each influence factor affecting the connectivity. By using the normalization method, the contribution of parent and child sequences to connectivity can be comprehensively considered. The normalization formula is

$$a_i = r_{i,0} / \sum_{i=1}^{n} r_{i,0} \quad (14)$$

2.6.5. Calculation of Comprehensive Assessment Factor. Based on the fuzzy comprehensive evaluation method, the weight value of each parameter obtained based on the basis of formula 9 is multiplied by the quantitative index of each parameter in the matrix of formula 8, namely, the trade-off value of the single index, q. The comprehensive factor, Q, affecting the connectivity can be obtained by adding the trade-offs of each single index, that is

$$q_t = a_i\{X_t^{(0)}(i)\},\ i = 1, 2, 3, \cdots, m;\ t = 1, 2, 3, \cdots, n \quad (15)$$

$$Q_t = \sum_{t=1}^{n} q_t,\ t = 1, 2, 3, \cdots, n \quad (16)$$

3. RESULTS

3.1. 3D Reconstruction and Heterogeneity Analysis of Coal Reservoir. By analyzing the relationship between REV size and coal porosity, it can be seen that when the REV size is 200 voxels, the porosity gradually tends to be stable. Therefore, the size of REV can be set at 200 voxels (Figure 9). Based on the scanning data and the reconstruction technology, the 3D visualization reconstruction of the coal sample can be realized, and the extraction and visualization of pore/fracture, matrix, and mineral in REV can be realized, respectively (Figure 9). The results of visualization reconstruction between samples show that the coal structure has high spatial heterogeneity. In REV, blue represents minerals, which are mainly distributed in the middle of the sample space with irregular shape. Gray represents the matrix, which is the largest proportion of coal. Red represents the pore/fracture, which is ellipsoidal and conical in various regions of the sample (Figure 9).

The volume fraction of each component in REV is calculated, and the calculation results are shown in Table 3. For the YW sample, the volume fractions of pore/fracture, matrix, and mineral are 10.67%, 60.62%, and 28.71%, respectively. For the SH sample, the volume fraction of pore/fracture, matrix, and mineral are 8.94%, 50.47%, and 40.59%, respectively. For the RL sample, the volume fraction of pore/fracture, matrix, and mineral are 10.63%, 35.70%, and 53.68%, respectively. For the PY sample, the volume fraction of pore/fracture, matrix, and mineral are 5.88%, 84.74%, and 9.38%, respectively (Table 3).

Previous studies have shown that when the porosity of coal reaches 15%, the fluid migration effect is the best.[11] In this study, the porosity of four coal samples is in the range of 5.88%−10.67% (Table 3), which indicates that porosity is the key factor restricting fluid migration and that coal samples with large porosity are more likely to form strong connectivity fractures, which is conducive to fluid seepage. The variation range of pore/fracture proportion among different samples is small with 5.88%−10.67%, while the variation ranges of organic matter with 35.70%−84.74% and mineral with 9.38%−53.68% are large (Table 3). The proportions of pore/fracture, matrix, and mineral also explain the heterogeneity of the coal reservoir.

3.2. 3D Visualization Reconstruction of Interconnected Pores and Fractures and Its Quantitative Analysis of Characteristic Parameters. After 3D visualization reconstruction of the coal reservoir, the interconnected pores/fractures can be further extracted from the pore/fracture network model (Figure 10). In the pore/fracture network model, the same color can be used to identify and analyze the same pore/fracture. Therefore, the connectivity of the pore/fracture can be well reflected in the 3D reconstruction model; that is, within the range of RVE, adjacent pore/fracture with uniform color coverage and large area indicate good connectivity of pore/fracture (Figure 10). The interconnected pores/fractures of YW and PY samples are mainly distributed in sheets and are mainly connected in the Z direction (Figure 10b, d). The interconnected pores/fractures of SH and RL samples are mainly distributed in bands, with good

https://doi.org/10.1021/acsomega.2c06943
ACS Omega 2023, 8, 11852−11867

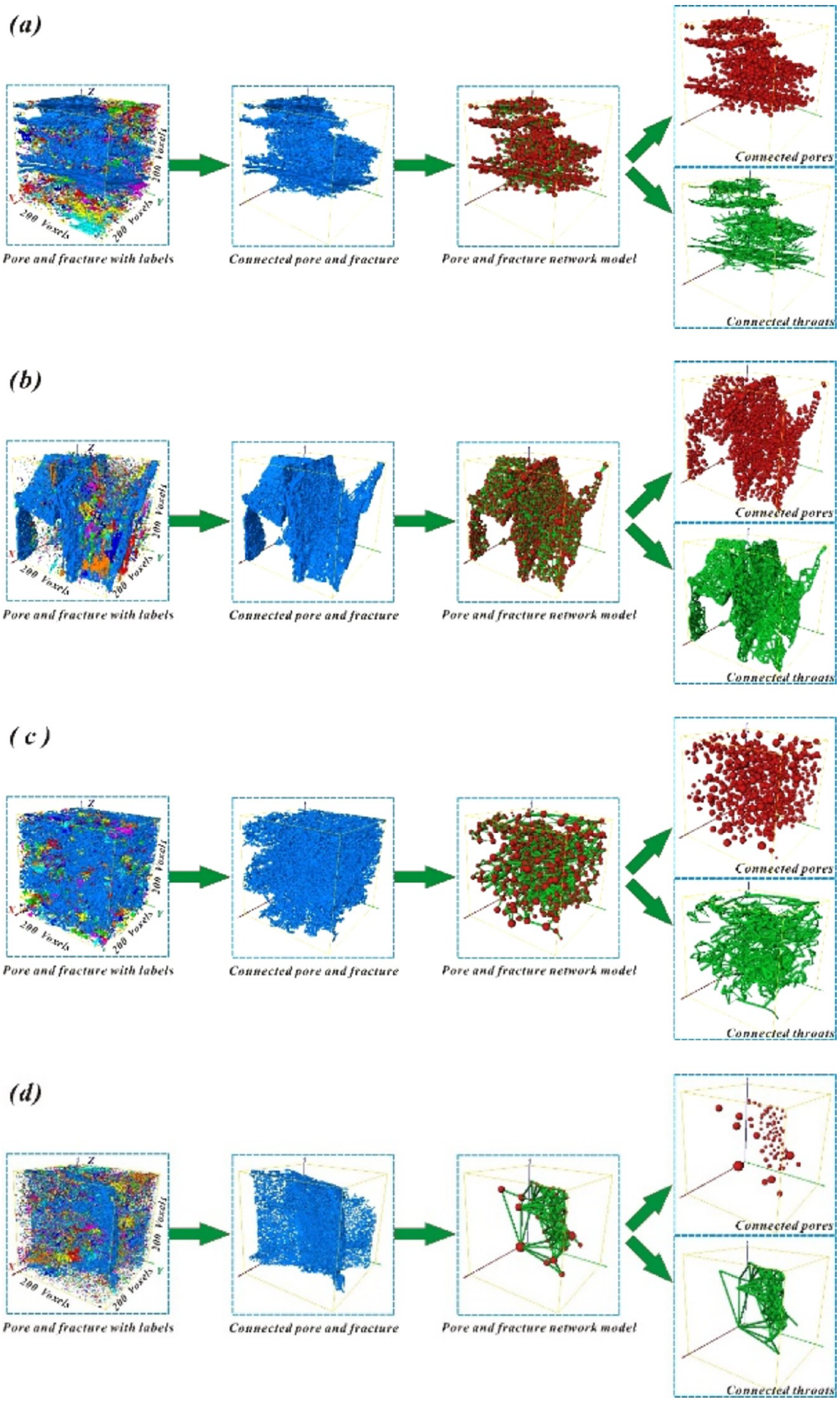

Figure 10. Visualization of connected pores/fractures and extraction of equivalent pore/fracture network model: (a) YW sample; (b) SH sample; (c) RL sample; and (d) PY sample.

https://doi.org/10.1021/acsomega.2c06943
ACS Omega 2023, 8, 11852−11867

connectivity in all three directions of the samples (Figure 10a, c). The spatial distribution pattern of connected pores/fractures has great influence on the porosity and permeability evolution of the coal reservoir.

In the equivalent pore/fracture network model, the interconnected pores and throats can be further extracted (Figure 10). The overall development and the quantitative equilibrium of pores and throats will further affect the connectivity of pores and fractures. According to the spatial distribution of the equivalent pore/fracture network model and the total and proportion of pores and throats, it can be seen that YW and SH samples have good connectivity and SH samples have the best connectivity (Figure 10a, b). The connectivity of the PL and PY samples was the next, and the connectivity of the PY sample was the worst (Figure 10c, d).

The geometric and topological characteristic parameters of pores and throats can be further extracted from the equivalent pore/fracture network model, which can be used to quantitatively analyze the influence of the characteristic parameters of the pore/fracture on its connectivity.

For the four samples, the coordination number was distributed in the range 1−15 (Figure 11), which indicates

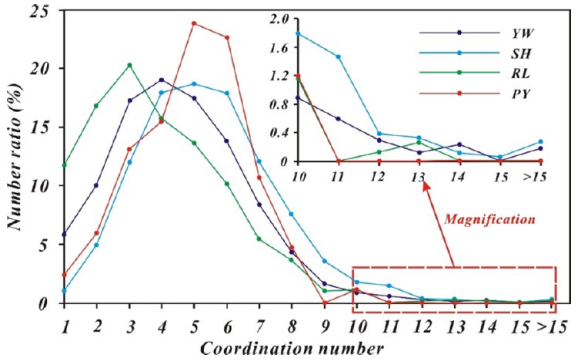

Figure 11. Range and proportion of coordination numbers for four samples.

that there were many throats connecting the pore/fracture, which enhanced the connectivity of the fracture network. The coordination numbers of the four samples were concentrated between 3 and 6, and the ratio in this range was 67.55%, 66.49%, 59.82%, and 75.00%, respectively (Figure 11), which indicates that most of the interconnected pores/fractures in the four samples were connected by 3−6 throats. The coordination number refers to the number of throats connected by pore/fracture, and its value can also indirectly reflect the proportion of pore/fracture and throat. Therefore, the smaller the fluctuation of the distribution curve of the coordination number, the more uniform the development of pores and throats and the better the connectivity of pores and fractures. It can be seen from Figure 11 that the curve fluctuation of coordination number of YW and SH samples is relatively moderate, while that of RL and PY samples is relatively large, so the connectivity of YW and SH samples is better than that of RL and PY samples. The pores/fractures in SH samples are relatively developed and extended in multiple directions of the coal sample, which can connect other isolated pores and fractures (Figure 10b) to maximize the total coordination number, which is 5.44, and the connectivity of the coal sample is the best. Due to the lack of connected throats between most of the pores and fractures (Figure 10d), the connectivity of the PY sample is still low, with an average coordination number of only 2.95.

In addition to porosity and coordination number, fracture size is also one of the main factors affecting the connectivity of the pore/fracture, and the corresponding parameter is the Ferret diameter. The range and its proportion of Ferret diameter of four samples are shown in Figure 12. The Ferret

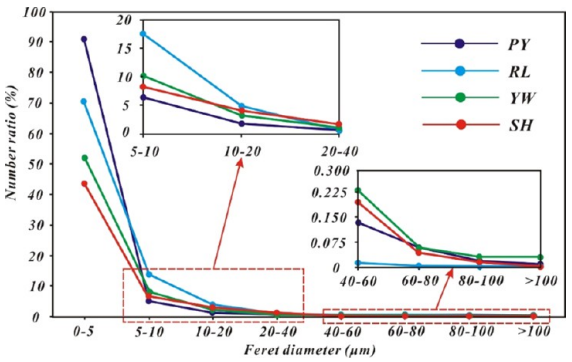

Figure 12. Various Feret diameter distributions for the four samples.

diameter was mainly 0−10 μm, and the proportions of the four samples in this range were 94.33%, 95.16%, 98.00%, and 91.50%, respectively. With the increase of the Ferret diameter, the number of pores/fractures presents an obvious downward trend (Figure 12). There is a positive correlation between the Ferret diameter and the pore/fracture connectivity. When the Ferret diameter is smaller, that is, 0−5 μm, the development of pore/fracture in PY and RL samples is better than that of the YW and SH samples. When the Ferret diameter is larger, that is, < 40 μm, the development of pore/fracture in YW and SH samples is better than that of RL and PY samples (Figure 12). Therefore, the overall connectivity of the pore/fracture in YW and SH samples is better than that in RL and PY samples. This research finding is in good agreement with the analysis conclusion of the coordination number.

As far as tortuosity is concerned, its value is inversely proportional to the connectivity, and the larger its value, the worse the connectivity of samples is. The tortuosity of YW, SH, RL, and PY samples is 2.27111, 1.9034, 3.98522, and 3.51516, respectively (Figure 13), which indicates that the connectivity of YW and SH samples is better than that of RL and PY samples, and the connectivity of SH sample is the best. Contrary to the indicative significance of tortuosity on connectivity, the size of the Euler characteristic number is proportional to pore/fracture connectivity, and the larger the

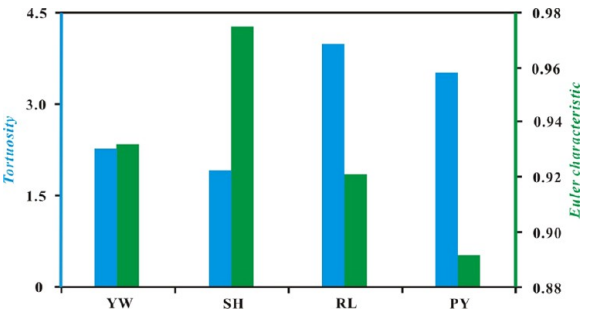

Figure 13. Distribution of tortuosity and Euler characteristic number of pore/fracture for four samples.

https://doi.org/10.1021/acsomega.2c06943
ACS Omega 2023, 8, 11852−11867

Table 4. Absolute permeability of four samples

Sample ID	Absolute permeability (μm^2)			
	X direction	Y direction	Z direction	Average value
YW	0.019063059	0.027269622	0.01072796	0.019020214
SH	0.021701647	0.019052723	0.022947419	0.02123393
RL	0.01396031	0.012494978	0.0082076378	0.011554309
PY	—	0.0095090773	0.0099458909	0.009727484

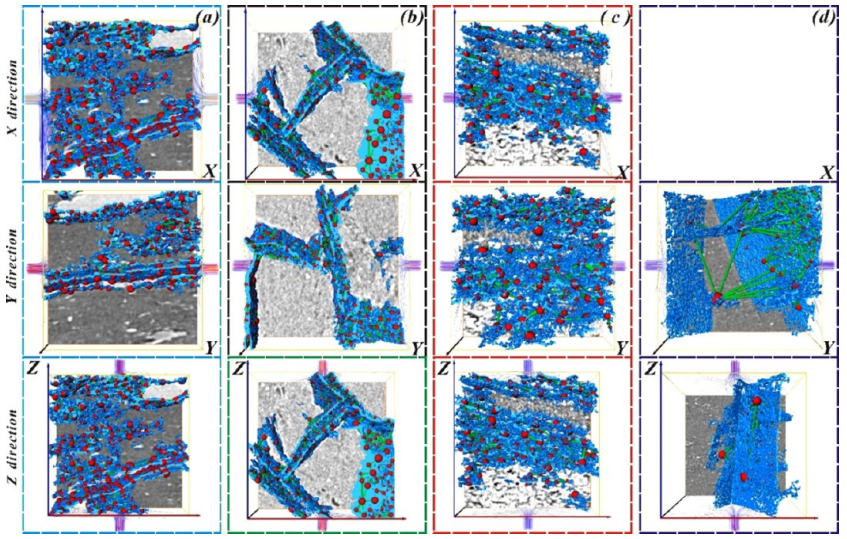

Figure 14. Superposition effect of fluid velocity field and connected pore/fracture network model of four samples: (a) YW sample; (b) SH sample; (c) RL sample; (d) PY sample.

value, the better the sample connectivity is. The Euler characteristic numbers of the YW, SH, RL, and PY samples are 0.931868, 0.974719, 0.921144, and 0.897697, respectively (Figure 13), which indicates that the connectivity of the YW and SH samples is better than that of the RL and PY samples, and that the connectivity of the SH sample was the best, while that of the PY sample was relatively poor.

3.3. Quantitative Analysis of Sample Permeability and Its Differential Characterization in Direction. The permeability of the coal reservoir is the most intuitive representation of the connectivity of pore/fracture. The interconnected pore/fracture extracted can be used as a geological carrier to carry out the numerical simulation. The analysis domain of the sample was 200 × 200 × 200 pixels, and the actual voxel of the sample was 200 × 200 × 200 μm^3.

The absolute permeability of the four samples in different directions is calculated, and the quantitative results are shown in Table 4. For the YW sample, the permeability of the *X* and *Y* directions is better than that of the *Z* direction. For the SH sample, the permeability in *X*, *Y*, and *Z* directions is good, and the permeability of the *X* and *Y* directions is better than that of the *Z* direction. For PY sample, the pores/fractures in the *X* direction have no connectivity, the permeability value is 0 μm^3, and the permeability in the *Y* and *Z* directions has certain development (Table 4; Figure 14). In terms of average permeability, the permeabilities of the SH and YW samples are higher than those of the RL and PY samples. The SH sample has the best permeability of 0.02123393 μm^3, while the PY sample has the worst permeability of 0.009727484 μm^3, and the PY sample is not connected in the *X* direction (Table 4).

The distribution condition of connected pores/fractures and the angle difference between them and each direction are two of the core factors affecting the sample permeability. Figure 14 shows the superposition effect of the fluid velocity field and the connected pore/fracture network model. It can be seen from Figure 14 that the connected pores/fractures of the YW sample are mainly banded in the *Y* direction and flake in the *X* and *Z* directions. The flowchart density of the velocity field is large in the *Y* direction and relatively small in the *X* and *Z* directions (Figure 14a). The interconnected pores/fractures of SH sample are mainly banded, and each band is connected in three directions, which can well explain that the permeability of SH sample has little difference in three directions, the overall permeability is good, and the density of flowchart of velocity field is uniform in three directions (Figure 14b). The connected pores/fractures of RL sample are distributed in the *X*, *Y*, and *Z* directions. Although the interconnected pores/fractures are distributed in the *Z* direction, their distribution direction is greatly different from that in the *Z* direction, which results in low permeability of sample in the *Z* direction and low density of flowchart of velocity field (Figure 14c). There is no interconnected pore/fracture in the PY sample in the *X* direction, and the distribution direction of the interconnected pore/fracture in the *Y* direction presents a large angle difference with that in the *Y* direction. The average coordination number in the *Z* direction is low, and the development of the throats is not obvious, which results in the low permeability of PY sample and the overall low density of the flowchart of the sample velocity field (Figure 14d).

3.4. Correlation Evaluation and Weight Analysis of Influence Factors Affecting Interconnected Pores and Fractures. Based on the above analysis, high porosity is the basis for the formation of strongly connected fractures. A higher average coordination number connects the throat to

https://doi.org/10.1021/acsomega.2c06943
ACS Omega 2023, 8, 11852−11867

Table 5. Original Data Set of Correlation Analysis of Influence Factors of Connected Pores and Fractures

Sample	Permeability (μm^2)	Porosity (%)	Coordination number	Tortuosity	Euler characteristic number	Ferret diameter
YW	0.019020214	10.67	4.591016548	2.27111	0.931868	3.87249
SH	0.02123393	8.944	5.435562806	1.9034	0.974719	4.17054
RL	0.011554309	10.63	3.911688312	3.98522	0.921144	3.69325
PY	0.009727484	5.883	2.952380952	3.51516	0.897697	2.67158

Table 6. Weight Values of Influence Factors of Connected Pores and Fractures

Weight coefficient	Permeability (μm^2)	Porosity (%)	Coordination number	Tortuosity	Euler characteristic number	Ferret diameter
a	0.2828598	0.12801724	0.19453194	0.06677624	0.15151199	0.17630284

Table 7. Weight of Single Index and Comprehensive Weight of Influencing Factors of Connected Pores/Fractures of Four Samples[a]

	Weight of single index						
Samples	Permeability (μm^2)	Porosity (%)	Coordination number	Tortuosity	Euler characteristic number	Ferret diameter	*Q*
YW	0.2534	0.1280	0.1643	0.0381	0.1449	0.1637	0.8923
SH	0.2829	0.1073	0.1945	0.03190	0.1515	0.1763	0.9444
RL	0.1540	0.1275	0.1400	0.0668	0.1432	0.1561	0.7875
PY	0.1296	0.07058	0.1057	0.0589	0.1426	0.1129	0.6203

[a]Notes: *Q*, comprehensive weight of influencing factors.

different fractures and improves the connectivity of the fracture network. A lower tortuosity can represent the shortest path of the fluid migration. A larger Euler characteristic number can represent the optimal migration path of the fluid connectivity. Larger Ferret diameters directly improve the reservoir connectivity. Reservoir permeability is the most intuitive characterization parameter for the development of connected pores and fractures. Therefore, in this study, the mean permeability was used as the parent sequence of the correlation analysis of the influencing factors of the connected pore/fracture. The child sequence of the correlation analysis of the influencing factors affecting the connected pore/fracture is the porosity, that is, the mean coordination number, the tortuosity, the Euler characteristic number, and the mean Ferret diameter. The original data set of the correlation degree estimation and weight analysis of the influence factors affecting connected pore/fracture in reservoir is shown in Table 5.

After comprehensive analysis based on the gray correlation degree method, the calculation results of correlation degree and weight coefficient of all comparison sequences are shown in Table 6. According to the degree of correlation between reservoir permeability and the five parameters that affect the connectivity of the pore/fracture, the order of the five parameters is as follows: average coordination number > Ferret diameter > Euler characteristic number > porosity > tortuosity (Table 6). Based on the fuzzy comprehensive evaluation method, the comprehensive weight values of the influencing factors of the interconnected pores/fractures in the YW, SH, RL, and PY Samples are 0.892303578, 0.944408763, 0.787534675, and 0.620311481, respectively (Table 7). The fitting of the permeability value and comprehensive weight value is shown in Figure 15. It can be seen that the development trend of permeability is highly consistent with the comprehensive score calculated by influencing parameters, which indicates that connectivity parameters have a strong correlation with coal permeability (Figure 15). Generally speaking, there are more interconnected pores and fractures in the highly permeable coal samples.

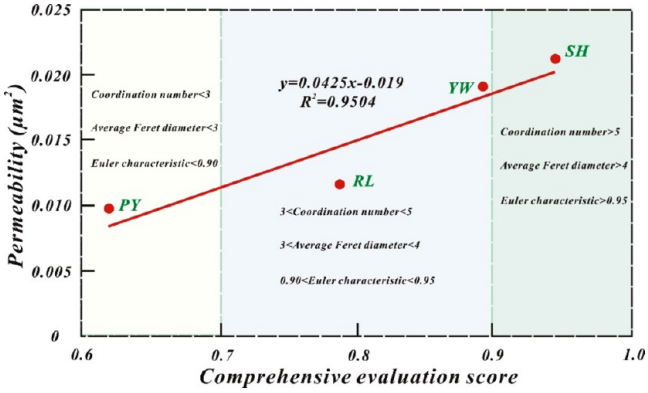

Figure 15. Fitting between permeability and comprehensive evaluation score.

Based on the first three characteristic parameters that affect the connectivity of connected pores and fractures in Table 6, the analysis area of the comprehensive evaluation score Q_t and the reservoir permeability value can be divided into three areas. Area 1: Q_t > 0.9, such as the SH sample, the average coordination number of the coal reservoir is >5, the Ferret mean diameter is >4, the Euler characteristic number is >0.95 (Figure 15). This kind of coal seam has good permeability and is mainly developed in the Qinshui basin. Area 2: 0.7 < Q_t < 0.9, such as the YW and RL samples, the average coordination number of this kind of coal reservoir is 3−5, the average Ferret diameter is 3−4, and the Euler characteristic number is 0.90−0.95 (Figure 15). This kind of coal seam has a moderate permeability. Area 3: Q_t < 0.7, such as the PY sample, the average coordination number of this coal reservoir is <3, the average Ferret diameter is <3, and the Euler characteristic number is <0.90 (Figure 15). This coal seam has poor permeability, especially in the Huainan and Huaibei coal field areas.

https://doi.org/10.1021/acsomega.2c06943
ACS Omega 2023, 8, 11852−11867

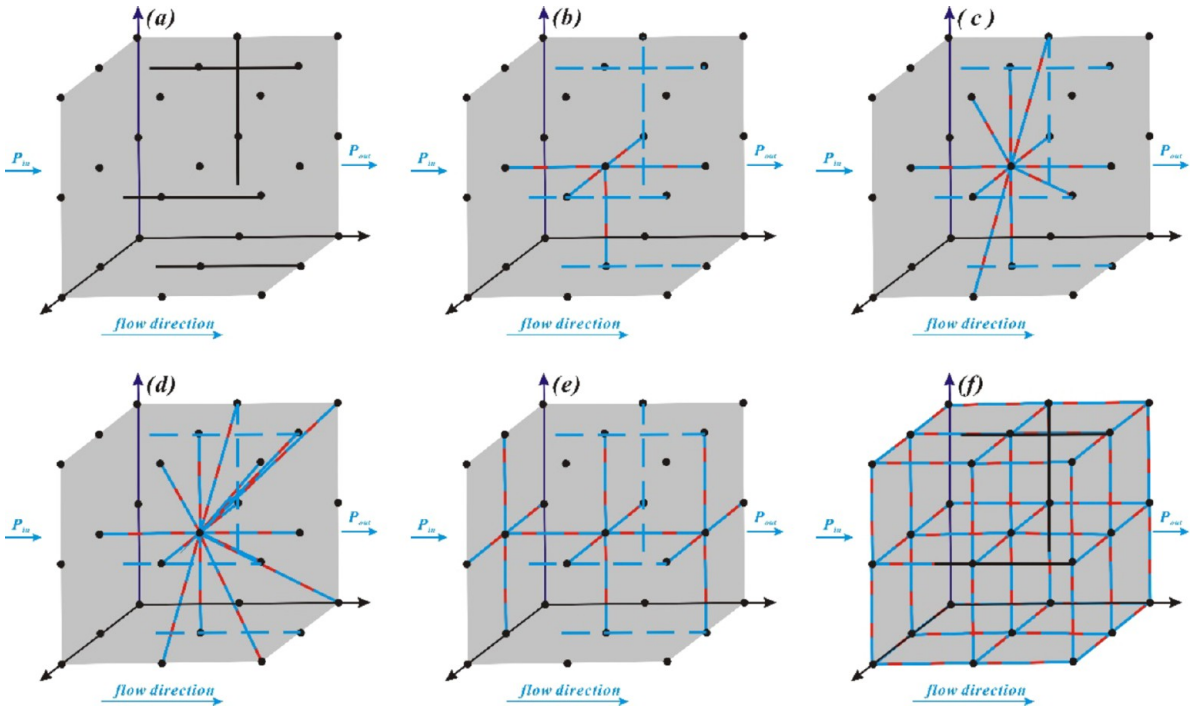

Figure 16. Schematic diagram of the influence of coordination number on the connectivity of pore/fracture. (a, b) represents the difference in coordination number; (e, f) represents the quantitative equilibrium of pores and throats.

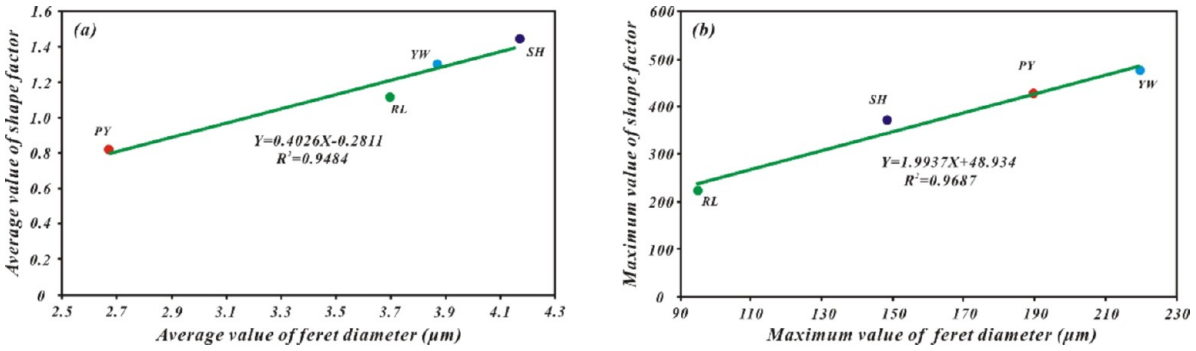

Figure 17. Relationship of ferret diameter and shape factor: (a) average value; (b) maximum value.

4. DISCUSSIONS

4.1. Schematic Analysis of Influencing Factors Affecting Pore and Fracture Connectivity at the Level of Structural Characteristics. *4.1.1. Coordination Number.* The 3D dual network model of pores/fractures is a dual media model with microscale, which contains the basic units of pores, throats, and microfractures, which can represent the pores, throats connecting pores, and microfractures in actual gas reservoirs, respectively (Figure 16). In Figure 16, black spheres represent pores, black columns represent microfractures, red columns represent growls (some of the red is covered by blue), and blue dotted lines represent areas of fluid activity. P_{in} is the inlet pressure, P_{out} is the outlet pressure, and the blue arrow represents the direction of fluid migration (Figure 16).

Taking the intermediate pore in Figure 16 as an example, the influence of the coordination number on pore/fracture connectivity was analyzed. From Figure 16a to Figure 16d, the coordination numbers are 0, 5, 10, and 15, respectively. The number of throats connected by the intermediate pores gradually increases. Among them, the coordination number of the pores not connected by throats is 0, and they are dead-ending pores. Because of the existence of throats, which play a good role in the communication of pores and microfractures, and with the increase of coordination number, the connected region of the sample gradually expands. The better the connectivity of the sample, the wider the movable region of the fluid is (Figure 16).

Figure 16d, f is used to analyze the influence of the quantitative equilibrium of the pores and throats on the connectivity. In Figure 16d, the quantity balance between pores and throats is poor, and the number of throats is significantly more than the number of pores and fractures. It can be found that the fluid movement area is limited to the outlet side of the model and the connectivity of pore and fracture in the sample is limited to the right side of the model (Figure 16d). In Figure 16f, the quantity of pores and throats is well balanced, and the number of throats is roughly equivalent to the number of pores and fractures. Fluid activity areas are all over the whole model, and the connectivity of pores and fractures in the sample is good (Figure 16f).

4.1.2. Ferret Diameter. The contribution of pores and fractures with larger Ferret diameter to their connectivity is

https://doi.org/10.1021/acsomega.2c06943
ACS Omega 2023, 8, 11852−11867

mainly reflected in the following two aspects: (1) they are interconnected with the connected pores and fractures to enhance the connectivity path of the connected pores and fractures; (2) the isolated pores and fractures are interconnected to become connected bridges to improve the connectivity of samples.

Considering that the Ferret diameter can represent the length of the fracture extending in a certain direction and the shape factor can also well represent the shape of pores and fractures in a certain direction, the relationship between the Ferret diameter and the shape factor can be drawn to explore the relationship between the extension distance of pores and fractures and the shape factor (Figure 17). It can be seen that both mean and maximum values are positively correlated; that is, the shape factor increases gradually with the increase of Ferret diameter (Figure 17).

Based on this, the study on the influence of Ferret diameter on connectivity of pore and fracture can be transferred to that of shape factor on its connectivity (Figure 18). With the

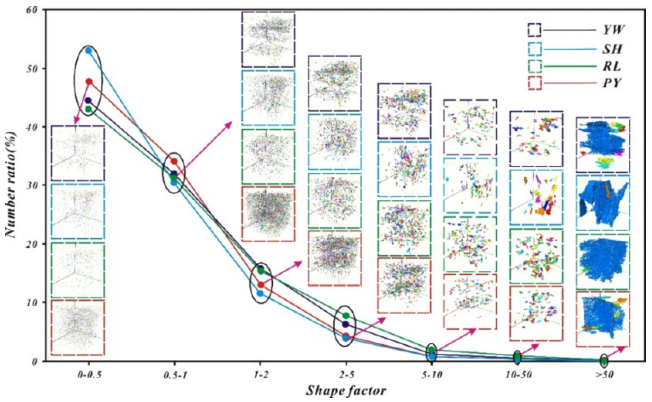

Figure 18. Proportion of the number of fractures with different shape factors (average value) for four samples.

increase of the shape factor, the numbers of pores and fractures gradually decreases and the extension distance gradually increases. When the shape factor is the largest value, the corresponding pores and fractures contribute more to the connectivity of the sample (Figure 18). When the shape factor reaches 50, the fracture can vertically penetrate the sample and the increase of the extension distance provides conditions for the formation of complex fractures (Figure 18). Complex fractures can better connect existing pores and fractures, thus increasing the connectivity of samples.

4.2. Application Discussion of Influencing Factors Affecting Pore and Fracture Connectivity at the Level of Structural Characteristics. The change of permeability of the coal reservoir is the most direct expression of the good or bad connectivity of pore and fracture, and the change of permeability is related to the effective stress effect, CH_4 desorption shrinkage effect, and competitive adsorption effect of CO_2/CH_4 in the process of CBM direct mining and CO_2 injection mining. Therefore, these effect factors are also the key to directly affect the geometrical and topological structures of the pore and fracture, which is intuitively reflected in the influence of the coordination number, Ferret diameter, tortuosity, connectivity function, shape factor, and other parameters.

4.2.1. Discussion on the Relationship between the Evolution Mechanism of Permeability and the Characteristic Parameters of Pore and Fracture Structures during Cbm Direct Mining. Figure 19 shows the evolution mechanism of permeability in a reservoir when CBM is directly mined, where A2, A3, and A5 respectively represent the areas near and far away from the boreholes. The white area represents the matrix pores, which mainly represents the change of matrix permeability. The gray area represents the coal matrix, which is mainly affected by the contraction effect of CH_4 desorption. The blue area represents the fracture, which mainly represents the change of fracture permeability and is mainly affected by the effective stress and the contraction effect of CH_4 desorption (Figure 19).

When CBM is directly mined, the permeability of the coal reservoir is mainly affected by the effective stress effect and matrix shrinkage effect caused by CH_4 desorption (Figure 19). In the early stage of CBM exploitation, the effective stress of fractures increases due to the pressure relief at the boundary of boreholes, which inevitably leads to the decrease of fracture porosity and then the decrease of fracture permeability. The pressure relief of the borehole will also lead to CH_4 desorption. On the one hand, the desorption of CH_4 will cause the shrinkage of matrix and thus increase the porosity of matrix; on the other hand, the migration of free CH_4 into the fracture will increase the pressure in the fracture system, thus effectively compensating for the reduction of effective stress. In this stage,

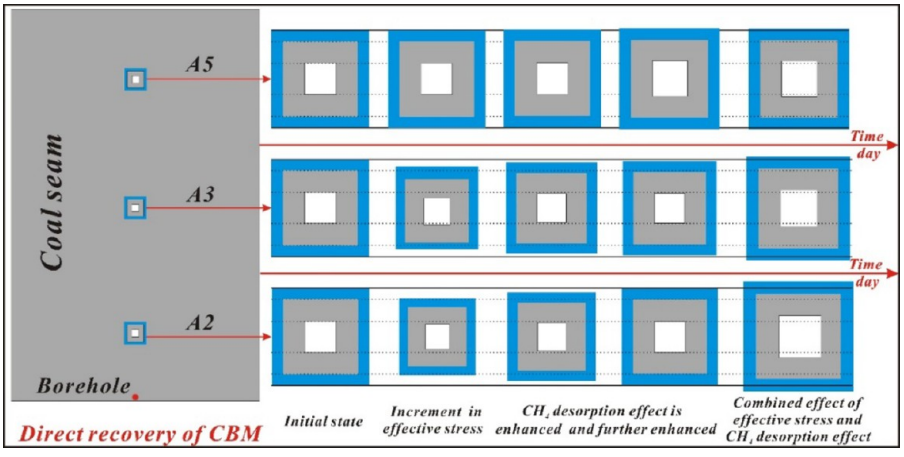

Figure 19. Evolution diagram of reservoir permeability in the process of CBM direct exploitation.

https://doi.org/10.1021/acsomega.2c06943
ACS Omega 2023, 8, 11852−11867

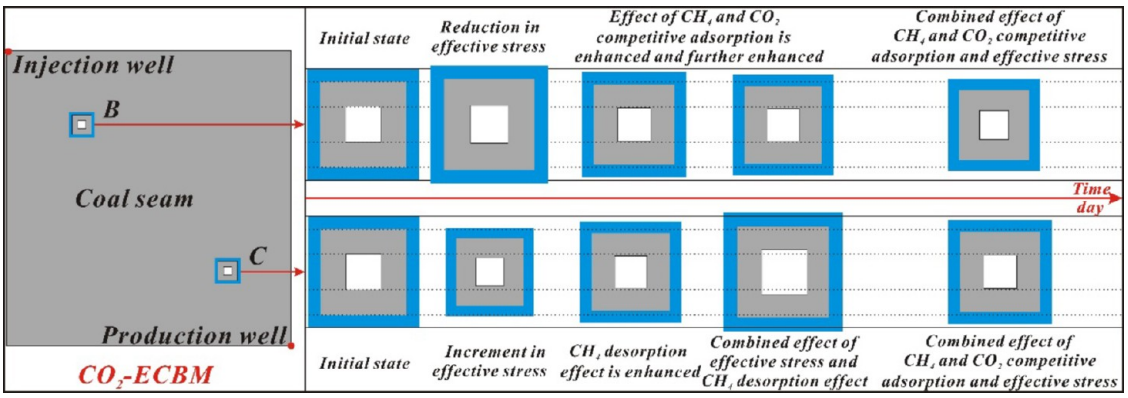

Figure 20. Evolution diagram of reservoir permeability during the CO_2-ECBM process.

the decrease of the coordination number, Ferret diameter, and shape factor and the increase of the tortuosity are concentrated, which has a negative effect on the connectivity of pores and fractures in the reservoir in a short time. With the increase of production time, the influence of CH_4 desorption on the porosity becomes more and more dominant. Under the combined action of CH_4 desorption and effective stress effects, both the fracture porosity and the matrix porosity are improved, and the increase is closer to the borehole (Figure 19). In this stage, the increases of the coordination number, Ferret diameter mean, tortuosity and shape factor have a positive impact on the connectivity of pores and fractures in the reservoir.

4.2.2. Discussion on the Relationship between the Evolution Mechanism of Permeability and the Characteristic Parameters of Pore and Fracture Structures during CO_2-ECBM Process. For the process of CO_2-ECBM, the evolution mechanism of permeability in a reservoir is shown in Figure 20. Point B represents the area near the gas injection well, and point C represents the area near the production well. The gray area represents the coal matrix, which is mainly affected by CH_4 desorption and competitive adsorption of CH_4 and CO_2. The pores in the outer blue area are mainly affected by the effective stress and competitive adsorption of CH_4 and CO_2. The connotations of other legends are consistent with those of Figure 19 (Figure 20).

In the CO_2-ECBM process, the change of reservoir permeability is mainly influenced by the effective stress effect and the competitive adsorption effect of CH_4 and CO_2 (Figure 20). In the area near the gas injection well, the CO_2 injection will reduce the effective stress, improve fracture porosity, and then lead to the increase of fracture permeability. However, at the same time, injected CO_2 will produce competitive adsorption with CH_4. Since the coal matrix preferentially absorbs CO_2, and the adsorption amount is often much larger, the injected CO_2 will cause great expansion of the matrix, which will reduce the permeability of the matrix. At the same time, the matrix swelling effect caused by the competitive adsorption of CH_4 and CO_2 has a more important influence on reservoir permeability than the effective stress effect, and the main body becomes more and more important (Figure 20). Therefore, when the CO_2 injection is used to extract CBM, the permeability of the area near the gas injection well gradually decreases, and the closer it is to the gas injection well, the more the permeability decreases. At this time, the decrease of the coordination number, Ferret diameter, and shape factor and the increase of the tortuosity are concentrated, which has a negative impact on the connectivity of the pore and fracture in the reservoir. In the area near the production well, when the injected CO_2 does not spread to this area, the permeability evolution mechanism is similar to that of the direct exploitation of the CBM (Figure 20). At this stage, it is concentrated in the increase of the coordination number, Ferret diameter, and shape factor and the decrease of tortuosity, which has a positive influence on the connectivity of the pore and fracture in the reservoir. When CO_2 injection began to spread to the region, the permeability evolution mechanism was similar to that of the region near the gas injection well when CO_2 injection was used to exploit CBM (Figure 20), which resulted in the gradual decrease of permeability in the later stage.

5. CONCLUSIONS

In this study, the YW, SH, RL and PY collieries are selected as the research areas. First, the 3D reconstruction of the coal structure can be realized. Second, the characteristic parameters of geometric and topological structures of pores/fractures are analyzed. Next, the absolute permeability and its characteristics are analyzed, and then the correlation and weight analysis of the influencing factors are realized. Finally, the schematic analysis and application discussion of the influencing factors are carried out. The main conclusions are as follows:

(1) Based on the 3D reconstruction of samples, the pore/fracture, matrix, and mineral can be extracted from REV. Porosity is the key factor restricting fluid migration. The variation range of the pore/fracture proportion is small, but the variation range of the organic and mineral proportion is large, which can represent the heterogeneity of the reservoir. The connected pores/fractures are mainly distributed in sheets and bands, which have different degrees of connectivity in different directions. The connectivity of the YW and SH samples is better than that of the RL and PY samples, and the connectivity of the SH sample is the best, while the connectivity of the PY sample is relatively poor.

(2) The coordination number is distributed in the range of 1 to 15. The Ferret diameter is 0−10 μm. The tortuosity is 2.27111, 1.9034, 3.98522 and 3.51516, respectively. The Euler characteristic number is 0.931868, 0.974719, 0.921144, and 0.897697, respectively. The permeability of the SH and YW samples is higher than that of the RL and PY samples. The permeability of the SH sample is the best with 0.02123393 μm^3, the permeability of the

https://doi.org/10.1021/acsomega.2c06943
ACS Omega 2023, 8, 11852−11867

PY sample is the worst with 0.009727484 μm^3, and the PY sample is not connected in the *X* direction.

(3) The single weight of each influence parameter affecting the connected pore/fracture from high to low is as follows: coordination number (0.19453194) > Ferret diameter (0.17630284) > Euler characteristic number (0.15151199) > porosity (0.12801724) > tortuosity (0.06677624). The comprehensive weight values of the four samples were 0.892303578, 0.944408763, 0.787534675, and 0.620311481, respectively. Based on the average coordination number, Ferret diameter, and Euler characteristic number, the comprehensive score of the influencing factors of the connected pores and fractures and the analysis region of the permeability value can be divided into three grades.

(4) The coordination number value and the quantity equilibrium of the pore/throat are positively correlated with the connectivity. With the increase of the Ferret diameter, the shape factor increases, the number of pores/fractures decreases, and the extension distance of the pore/fracture increases. The change of permeability is related to effective stress, CH_4 desorption shrinkage, and CO_2/CH_4 competitive adsorption, which is directly influenced by the coordination number, Ferret diameter, tortuosity, Euler characteristic number, and shape factor.

AUTHOR INFORMATION

Corresponding Author

Huihuang Fang − *School of Earth and Environment, Anhui University of Science and Technology, Huainan, Anhui 232001, China; Institute of Energy, Hefei Comprehensive National Science Center, Hefei 230000, China; Department of Geological Sciences, University of Saskatchewan, Saskatoon, SK S7N 5E2, Canada;* orcid.org/0000-0002-1139-5525; Email: huihuangfang@aust.edu.cn

Authors

Zhangfei Wang − *School of Earth and Environment, Anhui University of Science and Technology, Huainan, Anhui 232001, China; Institute of Energy, Hefei Comprehensive National Science Center, Hefei 230000, China*

Shuxun Sang − *Carbon Neutrality Institute and Jiangsu Key Laboratory of Coal-based Greenhouse Gas Control and Utilization, China University of Mining and Technology, Xuzhou 221008, China; School of Resources and Geosciences, China University of Mining and Technology, Xuzhou 221116, China*

Shiqi Liu − *Carbon Neutrality Institute and Jiangsu Key Laboratory of Coal-based Greenhouse Gas Control and Utilization, China University of Mining and Technology, Xuzhou 221008, China; School of Resources and Geosciences, China University of Mining and Technology, Xuzhou 221116, China;* orcid.org/0000-0003-1443-2675

Chengchuan Gu − *School of Earth and Environment, Anhui University of Science and Technology, Huainan, Anhui 232001, China*

Jing Yang − *Chongqing No.136 Geological Exploration Team, Chongqing 401147, China*

Lei Li − *The Third Exploration Team of Shandong Coalfield Geologic Bureau, Taian 250102, China*

Yanhui Huang − *State Key Laboratory of Petroleum Resources and Prospecting, China University of Petroleum, Beijing 102249, China; School of Earth and Environment, Anhui University of Science and Technology, Huainan, Anhui 232001, China*

Complete contact information is available at: https://pubs.acs.org/10.1021/acsomega.2c06943

Notes

The authors declare no competing financial interest.

ACKNOWLEDGMENTS

We express our gratitude to the anonymous reviewers for offering their constructive suggestions and comments that improved this manuscript in many aspects. This work was financially supported by the National Natural Science Foundation of China (No. 42102217), the University Synergy Innovation Program of Anhui Province (No. GXXT-2021-018), the Natural Science Research Project of Anhui University (No. KJ2020A0315; No. KJ2020A0317), and the Natural Science Foundation of Anhui Province (No. 2108085MD134).

REFERENCES

(1) Ni, H.; Liu, J.; Chen, T.; Chen, S.; Meng, Q. Coal permeability prediction method based on the microscopic pore-fracture dual-porosity structure. *J. Petrol. Sci. Eng.* **2022**, *211*, 110107.

(2) Liang, W.; Wang, J.; Sang, S.; Li, P. The influence of closed pores and stacked coal grains on gas transport in CO_2 injection enhanced CH_4 recovery process. *J. Petrol. Sci. Eng.* **2022**, *212*, 110303.

(3) Fang, H.; Sang, S.; Du, Y.; Liu, H.; Xu, H. Visualization characterization of minerals touched by interconnected pores and fractures and its demineralization effect on coal permeability during CO_2-ECBM process based on X-ray CT data. *J. Nat. Gas Sci. Eng.* **2021**, *95*, 104213.

(4) Liu, S.; Sang, S.; Hu, Q.; Fang, H. Characteristics of high-rank coal structure parallel and perpendicular to the bedding plane via NMR and X-ray CT. *Petrol. Sci.* **2020**, *17* (4), 925−938.

(5) Zhang, K.; Wang, S.; Wang, L.; Cheng, Y.; Li, W.; Han, X.; Liu, C.; Su, H. 3D visualization of tectonic coal microstructure and quantitative characterization on topological connectivity of pore-fracture networks by Micro-CT. *J. Petrol. Sci. Eng.* **2022**, *208*, 109675.

(6) Li, X.; Fu, X.; Tian, J.; Liu, X.; Ge, Y.; Wang, M.; Liang, S.; Wang, W. Invaded water flow back capability of high volatile bituminous coal after nitrogen displacing: from a perspective of fracture and seepage pore structural complexities. *Int. J. Oil Gas Coal T.* **2021**, *28* (2), 210−234.

(7) Yang, Y.; Yu, K.; Ju, Y.; Hu, Q.; Yu, B.; Qiao, P.; Chen, L.; Zhang, P.; Liu, F.; Song, Y.; Ju, L.; Li, W. Investigation on the structure and fractal characteristics of nanopores in high-rank coal: implications for the methane adsorption capacity. *J. Nanosci. Nanotechno.* **2021**, *21* (1), 392−404.

(8) Ni, Z.; Lin, B.; Zhang, X.; Cao, X.; Zhong, L.; Gao, Y. Experimental study on the effect of high-voltage electrical pulses on the nanoscale pore structure of coal. *Fuel.* **2021**, *306*, 121621.

(9) Xiang, J.; Zhu, Y.; Wang, Y.; Chen, S.; Jiang, Z. Structural deformation and its pore-fracture system response of the Wufeng-Longmaxi shale in the Northeast Chongqing area, using FE-SEM, gas adsorption, and SAXS. *J. Nat. Gas Sci. Eng.* **2022**, *209*, 109877.

(10) Fang, H.; Sang, S.; Liu, S.; Du, Y. Methodology of three-dimensional visualization and quantitative characterization of nano-pores in coal by using FIB-SEM and its application with anthracite in Qinshui basin. *J. Petrol. Sci. Eng.* **2019**, *182*, 106285.

(11) Wang, G.; Chen, X.; Wang, S.; Chen, H. Influence of fracture connectivity and shape on water seepage of low-rank coal based on CT 3D reconstruction. *J. Nat. Gas Sci. Eng.* **2022**, *102*, 104584.

(12) Zhou, S.; Liu, D.; Cai, Y.; Yao, Y.; Li, Z. 3D characterization and quantitative evaluation of pore-fracture networks of two Chinese coals using FIB-SEM tomography. *Int. J. Coal Geol.* **2017**, *174*, 41−54.

(13) Li, Z.; Liu, D.; Cai, Y.; Ranjith, P.; Yao, Y. Multi-scale quantitative characterization of 3-D pore-fracture networks in bituminous and anthracite coals using FIB-SEM tomography and X-ray mu-CT. *Fuel.* **2017**, *209*, 43−54.
(14) Xia, X.; Govindan, K.; Zhu, Q. Analyzing internal barriers for automotive parts remanufacturers in China using grey-DEMATEL approach. *J. Clean. Prod.* **2015**, *87*, 811−825.
(15) Tian, G.; Zhang, H.; Feng, Y.; Wang, D.; Peng, Y.; Jia, H. Green decoration materials selection under interior environment characteristics: a grey-correlation based hybrid MCDM method. Renew. Sustain. *Energy Rev.* **2018**, *81*, 682−692.
(16) Fan, C.; Li, S.; Zhang, H.; Yang, Z. Rational boreholes arrangement of gas extraction from unloaded coal seam. *Adv. Civ. Eng.* **2018**, *2018*, 1501860.
(17) Liu, S.; Sang, S.; Wang, G.; Ma, J.; Wang, X.; Wang, W.; Du, Y.; Wang, T. 2017. FIB-SEM and X-ray CT characterization of interconnected pores in high-rank coal formed from regional metamorphism. *J. Pet. Sci. Eng.* **2017**, *148*, 21−31.
(18) Fang, H. H.; Sang, S. X.; Liu, S. Q.; Liu, S. P. Experimental simulation of replacing and displacing CH_4 by injecting supercritical CO_2 and its geological significance. *Int. J. Greenh. Gas Control.* **2019**, *81*, 115−125.
(19) Feng, S.; Wei, Q.; Li, X. Chemical composition variations of altered and unaffected coals from the Huaibei coalfield, China: implications for maturity. *Energies.* **2021**, *14* (11), 3028.
(20) Fang, H.; Sang, S.; Liu, S. Three-dimensional spatial structure of the macro-pores and flow simulation in anthracite coal based on X-ray mu-CT scanning data. *Petrol. Sci.* **2020**, *17* (5), 1221−1236.
(21) Li, Z.; Zhang, G. Fracture segmentation method based on contour evolution and gradient direction consistency in sequence of coal rock CT images. *Math. Probl. Eng.* **2019**, *2019*, 2980747.
(22) Jing, D.; Meng, X.; Ge, S.; Zhang, T.; Ma, M.; Tong, L. Reconstruction and seepage simulation of a coal pore-fracture network based on CT technology. *Plos One.* **2021**, *16* (6), No. e0252277.
(23) Wang, Y.; Shabaninejad, M.; Armstrong, R.; Mostaghimi, P. Deep neural networks for improving physical accuracy of 2D and 3D multi-mineral segmentation of rock micro-CT images. *Appl. Soft. Comput.* **2021**, *104*, 107185.
(24) Ni, X.; Miao, J.; Lv, R.; Lin, X. Quantitative 3D spatial characterization and flow simulation of coal macropores based on mu-CT technology. *Fuel.* **2017**, *200*, 199−207.
(25) Wang, G.; Jiang, C.; Shen, J.; Han, D.; Qin, X. 2019. Deformation and water transport behaviors study of heterogenous coal using CT-based 3D simulation. *Int. J. Coal Geol.* **2019**, *211*, 103204.
(26) Zhang, G.; Ranjith, P.; Perera, M.; Haque, A.; Choi, X.; Sampath, K. Characterization of coal porosity and permeability evolution by demineralisation using image processing techniques: A micro-computed tomography study. *J. Nat. Gas Sci. Eng.* **2018**, *56*, 384−396.
(27) Wang, G.; Han, D. Y.; Jiang, C. H.; Zhang, Z. Y. 2020. Seepage characteristics of fracture and dead-end pore structure in coal at micro- and meso-scales. *Fuel.* **2020**, *266*, 117058.
(28) Zhao, Y.; Sun, Y.; Liu, S.; Chen, Z.; Yuan, L. Pore structure characterization of coal by synchrotron radiation nano-CT. *Fuel.* **2018**, *215*, 102−110.
(29) Shi, X.; Pan, J.; Pang, L.; Wang, R.; Li, G.; Tian, J.; Wang, H. 3D microfracture network and seepage characteristics of low-volatility bituminous coal based on nano-CT. *J. Nat. Gas Sci. Eng.* **2020**, *83*, 103556.
(30) Jing, Y.; Armstrong, R.; Ramandi, H.; Mostaghimi, P. Topological characterization of fractured coal. *J. Geophys. Res-Sol. Ea.* **2017**, *122* (12), 9849−9861.
(31) Chu, Y.; Sun, H.; Zhang, D. Experimental study on evolution in the characteristics of permeability, deformation, and energy of coal containing gas under triaxial cyclic loading-unloading. *Energy. Sci. Eng.* **2019**, *7* (5), 2112−2123.
(32) Zhu, Q.; Wang, X.; Zuo, Y.; Pan, J.; Ju, Y.; Su, X.; Yu, K. Numerical simulation of matrix swelling and its effects on fracture structure and permeability for a high-rank coal based on X-ray micro-CT image processing techniques. *Energy Fuel.* **2020**, *34* (9), 10801−10809.
(33) Zhang, L.; Jing, W.; Yang, Y.; Yang, H.; Guo, Y.; Sun, H.; Zhao, J.; Yao, J. The Investigation of Permeability Calculation Using Digital Core Simulation Technology. *Energies.* **2019**, *12* (17), 3273.
(34) Wang, G.; Qin, X.; Han, D.; Liu, Z. Study on seepage and deformation characteristics of coal microstructure by 3D reconstruction of CT images at high temperatures. *Int. J. Min. Sci. Techno.* **2021**, *31* (2), 175−185.
(35) Xie, J.; Gao, M.; Liu, J.; Li, C.; Peng, G. Permeability-enhanced rate model for coal permeability evolution and its application under various triaxial stress conditions. *Arab. J. Geosci.* **2020**, *13* (17), 865.
(36) Ni, X.; Zhao, Z.; Wang, Y.; Wang, L. Optimisation and application of well types for ground development of coalbed methane from no. 3 coal seam in Shizhuang south block in Qinshui basin, Shanxi province, China. *J. Petrol. Sci. Eng.* **2020**, *193*, 107453.

https://doi.org/10.1021/acsomega.2c06943
ACS Omega 2023, 8, 11852−11867